ResearchGate

See discussions, stats, and author profiles for this publication at: https://www.researchgate.net/publication/327188746

Application of multivariate recursive nesting bias correction, multiscale wavelet entropy and AI-based models to improve future precipitation projection in upstream of the Heihe Ri...

Article *in* Theoretical and Applied Climatology · August 2018

DOI: 10.1007/s00704-018-2598-y

CITATIONS
0

READS
73

7 authors, including:

Linshan Yang
Northwest Institute of Eco-Environment and Resources, Chinese Academy of Scie…
19 PUBLICATIONS **75** CITATIONS

SEE PROFILE

Zhenliang Yin
Chinese Academy of Sciences
28 PUBLICATIONS **187** CITATIONS

SEE PROFILE

Xiaohu Wen
Chinese Academy of Sciences
41 PUBLICATIONS **716** CITATIONS

SEE PROFILE

Some of the authors of this publication are also working on these related projects:

Project Black carbon in the environment View project

Project Political economy of climate change adaptation and disaster View project

All content following this page was uploaded by Linshan Yang on 06 September 2018.

The user has requested enhancement of the downloaded file.

Theoretical and Applied Climatology
https://doi.org/10.1007/s00704-018-2598-y

ORIGINAL PAPER

Application of multivariate recursive nesting bias correction, multiscale wavelet entropy and AI-based models to improve future precipitation projection in upstream of the Heihe River, Northwest China

Linshan Yang [1,2] · Qi Feng [1] · Zhenliang Yin [1] · Xiaohu Wen [1] · Ravinesh C. Deo [1,3] · Jianhua Si [1] · Changbin Li [4]

Received: 21 March 2018 / Accepted: 12 August 2018
© Springer-Verlag GmbH Austria, part of Springer Nature 2018

Abstract
Accurate projection of future precipitation is a major challenge due to the uncertainties arising from the atmospheric predictors and the inherent biases that exist in the global circulation models. In this study, we employed multivariate recursive nesting bias correction (MRNBC) and multiscale wavelet entropy (MWE) to reduce the bias and improve the projection of future (i.e., 2006–2100) precipitation with artificial intelligence (AI)-based data-driven models. Application of the developed method and the subsequent analyses are performed based on representative concentration pathway (RCP) scenarios: RCP4.5 and RCP8.5 of eight Coupled Model Intercomparison Project Phase-5 (CMIP5) Earth system models for the upstream of the Heihe River. The results confirmed the MRNBC and MWE were important statistical approaches prudent in simulation performance improvement and projection uncertainty reduction. The AI-based methods were superior to linear regression method in precipitation projection. The selected CMIP5 outputs showed agreement in the projection of future precipitation under two scenarios. The future precipitation under RCP8.5 exhibited a significantly increasing trend in relative to RCP4.5. In the future, the precipitation will experience an increase by 15–19% from 2020 to 2050 and by 21–33% from 2060 to 2090.

1 Introduction

Global circulation models (GCMs) that consider the behavior of the Earth's interaction of atmosphere, ocean, and land surface in three dimensions (Sillmann et al. 2013), providing plausible future simulations of weather variables at global scales, are the most adapted tools for a range of climate change studies at regional scale (Knutti et al. 2010). However, GCMs cannot directly provide sufficient information for local-scale applications like water resources planning and future climate impact assessments and are unable to capture the significant features of climatic variability in sub-grids of GCMs (Salvi et al. 2013). Because GCMs provide smoothly varying output at coarse scale, which are tens of thousands of square kilometers in size, and, hence, do not represent the true picture of regional climate conditions, the sub-grid spatial heterogeneity is missing.

Downscaling techniques are applied using various methods associated to a GCM output with a primary purpose to generate climatic projections that match the resolution of the local-scale catchment (Gudmundsson et al. 2012), and aim for (1) provision of systematic spatial variations, such as the variation of climatological temperature with elevation, or of climatological precipitation from the windward side to the rain shadow of a mountain and (2) provision of day-to-day variations in space such as the occurrence of localized rainfall events or temperature inversions between valleys and nearby mountain. Most commonly, downscaling techniques include dynamical and statistical methods. Dynamical downscaling requires expensive and sophisticated computations nested within regional-scale predictive models (Kouhestani et al. 2016). Furthermore, the downscaling results rely very much on the initial and boundary conditions of the GCM output, and the systematic error encountered has been relatively obvious (Misra et al. 2003). By contrast, statistical downscaling methods aim to construct a

✉ Qi Feng
qifeng@lzb.ac.cn

1 Key Laboratory of Ecohydrology of Inland River Basin, Northwest Institute of Eco-Environment and Resources, Chinese Academy of Sciences, Lanzhou 730000, Gansu, China

2 University of Chinese Academy of Sciences, Beijing 100049, China

3 School of Agricultural, Computational and Environmental Sciences, Institute of Agriculture and Environment, University of Southern Queensland, Springfield, QLD 4300, Australia

4 College of Earth Environmental Sciences, Lanzhou University, Lanzhou 730000, Gansu, China

Published online: 23 August 2018

statistical relationship between large-scale GCM outputs and local weather variables without being computationally demanding, and being easily adaptable to local scales especially if sufficient historical observation data are available (Dabanlı and Şen 2017). Consequently, statistical downscaling methods, such as stochastic weather generators which are based on the probability density functions of data (Mehrotra et al. 2013; Wilks 1998), weather typing approaches which are based on the airflow direction/vorticity or a cluster analysis (Huth et al. 2008; Santos et al. 2016), and transfer function approaches which are based on establishing empirical relationship trying to translate directly GCM climatic variables into local scales using linear or nonlinear regression (Asong et al. 2016; Sarhadi et al. 2017), are commonly applied in a number of hydrological and atmospheric studies (e.g., Hassan and Harun 2012; Mehrotra et al. 2013; Wilby and Dawson 2013).

However, the bias between the GCM outputs and the observation (commonly using reanalysis data from the National Centers for Environmental Prediction/National Center for Atmospheric Research (NCEP/NCAR)) can significantly affect the downscaling accuracy and lead to poor predictability in practical applications (Maraun 2016). In addition, the uncertainties from different GCMs can also dramatically influence the projection results. To resolve this issue, post-processing of GCM outputs is normally a prerequisite step for improving the quality of GCM simulations. Mehrotra and Sharma (2015) proposed a multivariate recursive nesting bias correction (MRNBC) method by processing across different levels of temporal aggregation to impart the observed distributional and persistence properties at multiple time-scales. The MRNBC can fulfill the first aim of downscaling for present climate conditions simply by calibration to high resolution with effective improvements in the simulations, resulting in the downscaled local-scale climatic data. However, for the mountainous region where the sub-grid of GCMs is usually not smooth, only using bias correlation methods cannot meet the satisfied downscaling results. In other words, the second aim of downscaling can be fulfilled, depending strongly on the variable and region of interest. Thus, there is a need to establish the relation between bias-corrected variables and observed regional variables (e.g., *precipitation here*). Compared to traditional linear regression method, artificial intelligence-based data-driven models (e.g., support vector regression (SVR), extreme learning machine (ELM)) become more popular in predictive modeling, owing to their ability to capture nonlinear relationships between predictors and predictand (Sarhadi et al. 2017). Neural networks (NNs) and support vector machines (SVMs) consider different learning techniques in computational intelligence community (Huang 2015). Two key reasons behind may be as follows: (1) the slow gradient-based learning algorithms are extensively used to train neural networks, and (2) all the parameters of the networks are tuned iteratively by using such learning algorithms. NNs and SVMs play key roles in machine learning and data analysis (Huang 2015). SVM presents advancement over conventional artificial neural network models (Duhan and Pandey 2015), whereas the ELM model is a fast and efficient neuro-computational approach offering an improvement in its design and universal approximation capability (Yin et al. 2017).

How to identify the crucial information on large-scale predictors that are related to the predictand variables is the major issue that is deeply affecting the modeling results. The recent work of Sehgal et al. (2018) proposed the multiscale wavelet entropy (MWE), applying Morlet continuous wavelet transform to obtain the temporal multiscale variability of atmospheric variables in the form of wavelet coefficients in order to measure the entropy for the respective climatic scales. It can also be integrated with the *k*-means clustering approach to enable the modeler in identifying the spectral organization of this multiscale variability in terms of the MWE (Sarhadi et al. 2017). This method can potentially consider the information about the physical structure of the predictor dataset and capture the behavior of the variables and related information generated about the uncertainties at a given scale (Sehgal et al. 2018).

Thus, in this study, we adopted the combination of MRNBC and MWE methods to improve the projection performance and reduce the uncertainty from different GCMs and compared multiple linear regression (MLR), SVR, and ELM in terms of improving the accuracy of the downscaling process. The primary aims of this paper are (1) to propose and develop a new statistical downscaling framework for the simulation of local-scale precipitation including the bias correction, the dimensional reduction, and the subsequent modeling and validation processes; (2) to improve the performance of the projection with a post-processing combination of MRNBC and MWE and AI-based modeling by employing an ensemble of GCM outputs; and (3) to apply consequently to detect the projected local-scale precipitation in the upstream of the Heihe River, Northwest China.

2 Materials and method

2.1 Study area

The upstream of the Heihe River, lying between 99°~101° E and 38°~39° N with a total surface area of 10,009 km^2, was selected as the primary domain for the present research, which is located in the north of Middle Qilian Mountain with great elevation variation from 5120 to 1674 m (Fig. 1). The climate is characterized by cold and moist conditions with large spatial and temporal heterogeneity. The average annual precipitation is more than 400 mm, and it increases by 15.5–16.4 mm for every 100 m increase in elevation (Yang et al. 2017a). The annual total runoff is 16.05×10^8 m^3 with a significant inter-annual variability (Yang et al. 2017b). It is the main region for

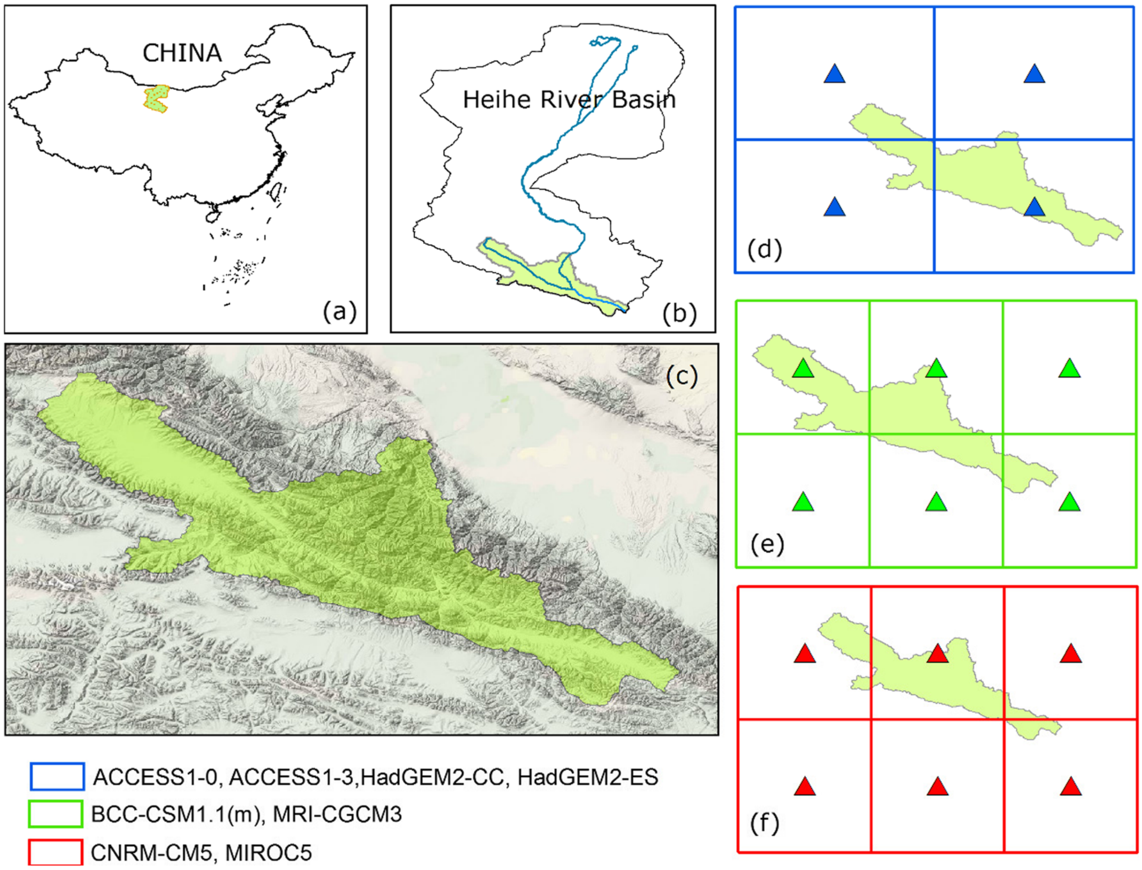

Fig. 1 **a** Location of the Heihe River in China. **b** Location and **c** distribution of the upper stream of the Heihe River. **d** GCM points and grids of ACCESS1.0, ACCESS1.3, HadGEM2-CC, and HadGEM2-ES. **e** GCM points and grids of BCC-CSM1.1(m) and MRI-CGCM3. **f** GCM points and grids of CNRM-CM5 and MIROC5

runoff generation in the entire Heihe River basin. About 90% of the water resources in the middle and lower reaches are therefore recharged by surface runoff from the headwater (Yin et al. 2017). The consistently evolving rapid expansion of the city and the population has led to severe environmental pressure, such as mismanagement and shortage of surface water resource, and this has attracted great attention in China (Feng et al. 2015). Therefore, the present study aims to investigate the impacts of future climate change on precipitation variability and the trends that are likely to impact the availability of surface water resources in this important socioeconomic region.

2.2 Datasets

To yield an extensive evaluation and applicability of the downscaling techniques, a set of eight projections of the atmospheric climate variables generated from the newest version of the Coupled Model Intercomparison Project Phase-5 (CMIP5) multimodel ensemble of the Fifth Assessment Report (AR5) of IPCC are adopted in this study. The basic information of the prescribed models is provided in Table 1. In order to train the model and validate the resulting simulations, the topographically corrected and regionally averaged monthly observation precipitation data ranging from 1960 to 2005 has also been employed.

In this study, the NCEP/NCAR reanalysis data are used to act as a proxy of the observed large-scale atmospheric predictors used in correcting systematic biases in the different GCMs and for developing the empirical model, which forms a basis for projecting the hydroclimatic predictand of particular interest (i.e., precipitation here). Therefore, a careful selection of the atmospheric predictors from the reanalysis data is extremely important, as they should be able to not only represent the climate change signals and demonstrate a significant association with the predictand but also must be realistically simulated by GCMs for future different climate change scenarios (Eghdamirad et al. 2017). In accordance with this notion, the primary atmospheric predictors identified in this study are shown in Table 2.

The future climate change simulations are thus employed for a period in the twenty-first century through different radiative forcing scenarios. It is important to note that the most recent climate change scenarios, known as the "representative concentration pathways" (RCPs), are designed to provide a consistent combination of the future population growth and

Table 1 Coupled Model Inter-comparison Project Phase-5 (CMIP5) model attributes selected in this study

Number	Model	Modeling center	Spatial resolution	Data length		
				Historical	RCP4.5	RCP8.5
1	ACCESS1-0	CSIRO-BOM (Australia)	1.875° × 1.25°	1948–2005	2006–2100	2006–2100
2	ACCESS1-3	CSIRO-BOM (Australia)	1.875° × 1.25°	1948–2005	2006–2100	2006–2100
3	BCC-CSMM	BCC (China)	1.125° × 1.125°	1948–2005	2006–2100	2006–2100
4	CNRM-CM5	CNRM-CERFACS (France)	1.400° × 1.400°	1948–2005	2006–2100	2006–2100
5	HadGEM2-CC	MOHC (UK)	1.875° × 1.25°	1948–2005	2006–2100	2006–2100
6	HadGEM2-ES	MOHC (UK)	1.875° × 1.25°	1948–2005	2006–2100	2006–2100
7	MIROC5	MIROC (Japan)	1.400° × 1.400°	1948–2005	2006–2100	2006–2100
8	MRI-CGCM3	MRI (Japan)	1.125° × 1.125°	1948–2005	2006–2100	2006–2100

social and economic developments with the specified radiative forcing pathways (Taylor et al. 2012). Two radiative forcing scenarios considered in the present study are the RCP4.5, in which the radiative forcing is estimated to increase to about 4.5 W/m^2 by year 2100 and decline afterwards, and the RCP8.5 with a radiative forcing of 8.5 W/m^2 by year 2100.

Table 2 Atmospheric predictors selected from the GCMs with variable descriptions

No.	Variable	Description
1	Pr	Precipitation
2	T_{as}	Near-surface air temperature
3	T_{asmax}	Daily maximum near-surface air temperature
4	T_{asmin}	Daily minimum near-surface air temperature
5	P_{sl}	Sea-level pressure
6	R_{hs}	Near-surface relative humidity
7	U_{as}	Eastward near-surface wind
8	V_{as}	Northward near-surface wind
9	Va_7P	Northward wind at 700 hPa height
10	Va_5P	Northward wind at 500 hPa height
11	Ua_7P	Eastward wind at 700 hPa height
12	Ua_5P	Eastward wind at 500 hPa height
13	Hus_7P	Specific humidity at 700 hPa height
14	Hus_5P	Specific humidity at 500 hPa height
15	Zg_7P	Geopotential height at 700 hPa
16	Zg_5P	Geopotential height at 500 hPa
17	R_{lds}	Surface downwelling longwave radiation
18	R_{lus}	Surface upwelling longwave radiation
19	R_{sds}	Surface downwelling shortwave radiation
20	R_{sus}	Surface upwelling shortwave radiation
21	H_{fls}	Surface upward latent heat flux
22	H_{fss}	Surface upward sensible heat flux
23	Hur_7P	Relative humidity at 700 hPa height
24	Hur_5P	Relative humidity at 500 hPa height
25	R_{hum}	Near-surface relative humidity
26	S_{hum}	Near-surface specific humidity

2.3 Methodology

2.3.1 MRNBC for bias correction

MRNBC approach is applied to correct two types of time series (nonseasonal and seasonal) based on multivariate autoregressive modeling. The general idea is that for all timescales of interest, the GCM simulations are nested into the observed monthly, seasonal, and annual time series which are chosen from the NCEP/NCAR atmospheric reanalysis data. Before applying the nesting, both time series are standardized to have a mean of zero and a standard deviation of 1.

Giving a vector m predictor variables with i time steps $\mathbf{Z}$ ($m \times t$ matrix) at a local site, the lag-one autocorrelations and the lag-one and lag-zero cross correlations in the GCM simulations can be corrected to match the observed correlations in time and space (Sarhadi et al. 2016). Note that $\mathbf{Z}^{\mathbf{h}}$ denotes the observations and $\mathbf{Z}^{\mathbf{g}}$ denotes the GCM variables. The data are first standardized to construct a periodic time series $\hat{Z}_i^g$ which need to be modified to match the observation $\hat{Z}_i^h$. The standard multivariate autoregressive order 1 (MAR1) model for both the observed and the GCM data is expressed as follows (Salas et al. 1985):

$$\hat{Z}_i^h = C\hat{Z}_{i-1}^h + D\varepsilon_i \tag{1}$$

$$\hat{Z}_i^g = E\hat{Z}_{i-1}^g + F\varepsilon_i \tag{2}$$

In Eqs. (1) and (2), $\boldsymbol{C}$ and $\boldsymbol{D}$ are the lag-zero and lag-one cross correlation coefficient matrices for the observation $\hat{Z}_i^h$. $\boldsymbol{E}$ and $\boldsymbol{F}$ are calculated by the same way for the standardized

GCM outputs, and ε_i is a vector of mutually independent random variation having zero mean and the identity covariance matrix. Rearrange the terms of the above equations (i.e., Eqs. (1) and (2)) and modify $\hat{Z}_i^g$ along with the lag-zero and lag-one correlation matrices (i.e., $\boldsymbol{C}$ and $\boldsymbol{D}$) to Z'^g_i that have the desired dependence properties (Salas et al. 1985)

$$Z'^g_i = CZ'^g_{i-1} + DF^{-1}\hat{Z}_i^g - DF^{-1}E\hat{Z}_{i-1}^g \tag{3}$$

For the correction of periodic parameters, let vectors $Z_{t,i}^h$ and $Z_{t,i}^g$ represent the observed and the GCM outputs, respectively, with m variables for the particular month i and year t. The standardized periodic time series with a mean of zero and a unit variance is denoted as $\hat{Z}_{t,i}$. Following Eq. (3), the series $Z'^g_{t,i}$ which maintains the observed lag-one serial and the cross dependence can be formulated as follows (Salas et al. 1985):

$$Z'^g_{t,i} = C_i Z'^g_{t,i-1} + D_i F_i^{-1}\hat{Z}_{t,i}^g - D_i F_i^{-1} E_i \hat{Z}_{t,i-1}^g \tag{4}$$

In Eq. (4), $Z'^g_{t,i-1}$ is the corrected time series from the previous mouth in year t. After the correction, the resulting time series Z'^g is rescaled by the observed mean and the standard deviation to yield the final corrected time series $\overline{Z}^g$. Further details of this approach can be found in the studies of Mehrotra and Sharma (2015) and Sarhadi et al. (2016).

Following the corrections to the monthly data, the time series $\overline{Z}^g$ is aggregated to generate the seasonal series and the periodic corrections described above are then applied, now indexed over the four seasons rather than the 12 months to yield $\overline{S}^g$ where $\boldsymbol{S}$ refers to the seasonal matrix of simulations (i.e., $p \times n/4$ in size). This time series is then aggregated to the annual time series, and the correlations, standard deviations, and mean data are corrected to form $\overline{A}^g$ (where $\boldsymbol{A}$ is the matrix of yearly data, $p \times n/12$). Subsequently, each time, aggregation corrections can be applied to the daily time series to create a simple correction step as follows (Srikanthan and Pegram 2009):

$$\overline{Z}_{i,j,s,t}^g = \left(\frac{\overline{Y}_{j,s,t}^g}{Y_{j,s,t}^g}\right) \times \left(\frac{\overline{S}_{s,t}^g}{S_{s,t}^g}\right) \times \left(\frac{\overline{A}_t^g}{A_t^g}\right) \times Z_{i,j,s,t}^g \tag{5}$$

In Eq. (5), $\overline{Y}_{j,s,i}^g$, $\overline{S}_{s,i}^g$, and $\overline{A}_i^g$ respectively denote the monthly, seasonally, and annually corrected values, and $Y_{j,s,i}^g$, $S_{s,i}^g$, and A_i^g respectively denote the aggregated monthly, seasonal, and annual values. The subscript i stands for day, j for month, s for season, and t for year.

A three-step correction procedure is used to correct biases firstly in the mean, then the standard deviation, and it finally applied the correlations. This ensures that the future climate change signal is not affected by the bias correction procedure that has been applied (Mehrotra and Sharma 2015).

2.3.2 *k*-means clustering-based principal component analysis

Due to the approximation of the statistical properties of the neighbor grid cells inducing some degree of redundancy and collinearity among predicted variables, the modeling procedure can give rise to inadequate results in terms of the performance accuracy. Therefore, we apply the *k*-means clustering-based principal component analysis (PCA) to preserve the information across different variables. This approach is also important to reduce the dimension of the predictors and further improve the prediction accuracy in the statistical downscaling process.

k-means clustering is an unsupervised learning algorithm of vector quantization, originating from a signal processing area as a popular tool for cluster analysis applied in data mining (Sehgal et al. 2018). It aims to partition n observations into k clusters in which each observation belongs to the cluster with the nearest mean, serving as a prototype of the cluster (Sarhadi et al. 2017). The basic idea of the *k*-means clustering is that, given an initial but not optimal clustering (k centroids), the approach relocates each point to its new nearest center and updates the clustering centers by calculating the mean of the member points and then repeating the relocating-and-updating process until converge criteria (such as the predefined number of iterations and the difference on the value of the distortion function) are satisfied (Macqueen 1967).

Given a set of observations (x_1, x_2 … x_n), where each observation is a d-dimensional real vector, the C_k represents the mean centroid of cluster k, which is defined as (Sehgal et al. 2018)

$$C_k = \frac{1}{N_k}\sum_{n=1}^{N_k} X_n \tag{6}$$

In Eq. (6), N_k denotes the number of feature vectors in cluster k. For each cluster, the PCA is applied to assign a set of candidate input variables and extract the principal components (PCs) which are orthogonal and, therefore, preserve most of the variance originally present in the variables (Kouhestani et al. 2016). Thus, in the dimensionality reduction procedure, the large-scale atmospheric predictors are imported into the *k*-PCA algorithms to generate a sequence of cluster-wise principal components which have maximal dependency with the target variable and then are employed as inputs for the downscaled model. More details on *k*-means clustering can be consulted from Hartigan and Wong (1979) and Jin and Han (2016).

2.3.3 MWE

In this study, we have utilized MWE as a substitute to represent the multiscale variations in the given time series (Agarwal et al. 2016b). The wavelet coefficients generated from the continuous wavelet transform analysis are utilized to obtain the multiscale wavelet entropy coefficient using the Shannon entropy measure given by

$$\mathrm{S}_{wt}(\mathrm{x}) = -\sum_{i=1}^{n} P(x_i)\ln(P(x_i)) \tag{7}$$

In Eq. (7), $P(x_i)$ is the probability distribution function to describe the random behavior of the variable x with a length of n. The multiscale entropy $\mathrm{S}_{wt}(\mathrm{x})$ represents the distribution of the certainty of a given process at different scales. The lower values of S indicate more information contained a higher predictable system. The value $P(x_i)$ is given by

$$P(x_i) = \frac{E(i,j)}{E(j)} = \frac{|W(i,j)|^2}{\sum|W(i,j)|^2} \tag{8}$$

where $E(i,j)$ represents the wavelet energy under time position i and timescale j and $E(j)$ represents the total wavelet energy of the time series under timescale j. For the given scale a, the multiscale entropy can be calculated as Sang et al. (2011)

$$S_a(x) = -\sum_{i=1}^{n} P\left(d_{a,i}\right)\ln\left(P\left(d_{a,i}\right)\right) \tag{9}$$

In Eq. (9), S_a represents the entropy of the given process at the timescale a, and $d_{a,\ i}$ denotes the detailed coefficients of the given process at scale a obtained using the wavelet transform. More details about MWE are provided in Agarwal et al. (2016a, 2016b). Figure 2 exemplifies the multiscale entropy process with wavelet coefficients and entropy at different scales using air temperature data.

The multiscale entropy signature is used as the basis to generate homogeneous clusters using the *k*-means clustering technique (Santos et al. 2016). Following this, we apply the PCA method to each cluster in order to obtain the input variables for the regression model. The input variables and observed precipitation are transformed into the respective wavelet sub-time series for three dyadic resolution levels using discrete wavelet transform (DWT) (Sturm 2007). The process consists of a number of successive filtering steps in which the time series is decomposed into approximation (A) and detailed sub-time series or wavelet components (D1, D2, D3, etc.). Approximation components represent the slowly changing coarse features of a time series and are obtained by correlating the stretched version (i.e., low-frequency and high-scale) of a wavelet with the original time series, while the detailed components signify rapidly changing features of the time series and are obtained by correlating the compressed wavelet (i.e., high-frequency and low-scale) with the original time series (Maheswaran and Khosa 2012).

2.3.4 MLR

In essence, the MLR algorithm attempts to model the relationship between the dimensionally reduced atmospheric predictors and the target variable at the downscaled local site by fitting a linear equation. Subsequently, the MLR model is defined as (Draper and Smith 1981; Montgomery et al. 2012)

$$Y_i = \beta_0 + \beta_1 X_{1,i} + \beta_2 X_{2,i} + \ldots + \beta_p X_{p,i} + \varepsilon_i \tag{10}$$

In Eq. (10), Y_i denotes the observed precipitation sub-time series, X denotes the independent sub-time variable matrices with

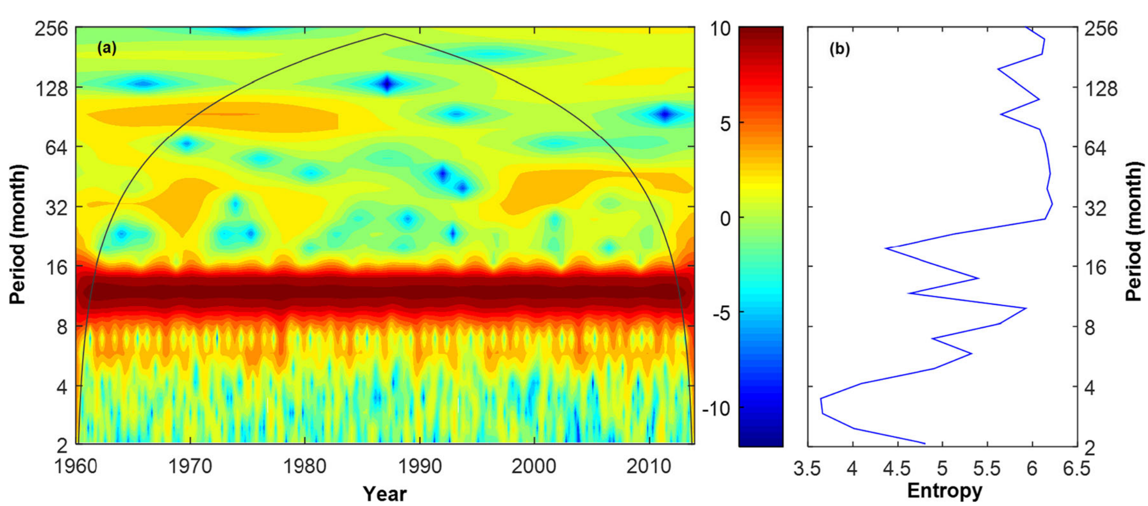

Fig. 2 Illustration of the multiscale entropy in air temperature data by means of **a** wavelet coefficients and **b** entropy values across the different scales

$p \times n$ in size, β denotes the regression coefficient matrices with $(p+1) \times n$ in size, and ε_i denotes the residual between the observational and fitted values. The downscaled value of precipitation is then reconstructed from the outputs of the MLR model by a linear summation of the outputs of each sub-time series.

2.3.5 Extreme learning machine

The ELM is a suite of neural network algorithms in which hidden neurons need not be tuned with the consideration of neural network generalization theory, control theory, matrix theory, and linear system theory (Huang 2015; Huang et al. 2004, 2006). Compared to ANN, the ELM shown better generalization performance and relatively faster learning speed than the conventional feed forward network (Deo and Şahin 2016; Deo et al. 2016; Yin et al. 2017). The ELM is an improved version of the ANN model with the input weight and the hidden layer threshold randomly assigned and the output layer weights directly calculated by the least square method (Patil and Deka 2016). Thus, the whole learning process is complete without iteration and achieves extremely fast learning speed (Abdullah et al. 2015; Gocic et al. 2016; Huang et al. 2006).

Given n training samples $\boldsymbol{X}i = [x_{i1}, x_{i2}, \cdots, x_{in}]^T$, the output function for SLFNs with L hidden nodes can be expressed as

$$f_L(\mathbf{x}) = \sum_{i=1}^{i=L} \beta_i h_i(\mathbf{x}) \tag{11}$$

where β_i is the output weight of the ith hidden node. $h_i(x)$ is the hidden layer output mapping of ELM, representing the randomized hidden features of predictor $\boldsymbol{X}_i$, and $h_i(\mathbf{x})$ is the ith nonlinear piece-wise continuous hidden layer activation function, given as

$$h_i(\mathbf{x}) = G(a_i, b_i, X) \tag{12}$$

where a_i and b_i are two hidden neuron parameters. The model's approximation error is minimized when solving for weights connecting the hidden and output layers (β) using a least square method, and its objective function is given as

$$\min_{\beta \in R^{L\times m}} \|\mathrm{H}\beta - \mathrm{T}\|^2 \tag{13}$$

where $\mathbf{H}$ is the hidden layer output matrix

$$\mathrm{H} = \begin{bmatrix} g(x_1) \\ \vdots \\ g(x_N) \end{bmatrix} = \begin{bmatrix} g_1(a_1x_1 + b_1) & \cdots & g_L(a_Lx_1 + b_L) \\ \vdots & \cdots & \vdots \\ g_1(a_Nx_N + b_1) & \cdots & g_L(a_Lx_N + b_L) \end{bmatrix} \tag{14}$$

$\mathbf{T}$ is the training target matrix

$$\mathrm{T} = \begin{bmatrix} \mathrm{t}_1^T \\ \vdots \\ \mathrm{t}_N^T \end{bmatrix} = \begin{bmatrix} t_{11} & \cdots & t_{1m} \\ \vdots & & \vdots \\ t_{N1} & \cdots & t_{Nm} \end{bmatrix} \tag{15}$$

2.3.6 Support vector regression

SVR is an algorithm of SVM usually used for solving the problem of small training data and nonlinear and high-dimensional pattern recognition (Vapnik 1995). The key of SVR is the kernel function to map to high-dimensional space and introducing the relaxation and penalty coefficients to calibrate the error between the kernel function and target data (Hamidi et al. 2015). For a given training $\mathbf{X}$, the input is first mapped onto a high-dimensional feature space $\phi(x)$ (kernel function), then a linear model is performed in these feature spaces (Hamidi et al. 2015); the vector linear expression can be as follows:

$$f(x) = \omega \cdot \phi(x) + b \tag{16}$$

where ω is the weight vector, b is a constant, and $\phi(x)$ is a mapping function set of nonlinear transformation. The coefficients ω and b can be estimated by trying to reduce the model complexity by minimizing

$$R_{\mathrm{reg}}(f) = C\frac{1}{N}\sum_{i=1}^{N} L_\varepsilon(f(x_i), y_i) + \frac{1}{2}\|w\|^2 \tag{17}$$

$$L_\varepsilon(f(x) - y) = \begin{cases} |f(x) - y| - \varepsilon & \text{for} |f(x) - y| \geq \varepsilon \\ 0 & \text{otherwise} \end{cases} \tag{18}$$

where both C and ε are the parameters to be determined which influence the generalization performance, and the quality of estimation is measured by the loss function $L_\varepsilon(f(x_i), y_i)$ which is called the ε-intensive loss function (Vapnik 1995).$C\frac{1}{N}\sum_{i=1}^{N} L_\varepsilon(f(x_i), y_i)$ denotes the empirical error. $\frac{1}{2}\|w\|^2$ denotes the smoothness of the function. C evaluates the trade-off between the empirical risk and the smoothness of the model (Yin et al. 2017). A Lagrange multiplier and optimality constraints are used, so the optimization problem can be transformed into the dual problem (Duhan and Pandey 2015), given as

$$f(x) = \sum_{i=1}^{l} (\alpha_i - \alpha_i^*) k(x_i, x) + b \tag{19}$$

where α_i and α_i* are the introduced Lagrange multipliers and $k(x_i, x)$ is the kernel function.

2.4 Precipitation projection framework and performance assessment

The flow chart for the downscaling precipitation framework is shown in Fig. 3. In this study, based on the MRNBC and MWE methods, we corrected the GCM variables by NCEP reanalysis data and obtained inputs to downscaling precipitation model. Then, we ran the SVR, ELM, and MLR models with observed historical precipitation as target and compared the downscaling performance levels of the historical precipitation derived from different downscaling methods. Finally, we applied the downscaling method to the upstream of the Heihe River with future climate change scenarios to detect the projected local-scale rainfall on future surface water availability and employed eight of CMIP5 Earth system models to reduce the uncertainty in future climate simulations.

We employed the coefficient of correlation (R), mean absolute error (MAE), root-mean-square error (RMSE), and the Nash-Sutcliffe efficient (NSE) as estimation performance evaluation matrices to assess the accuracy of historical precipitation simulation results (Chai and Draxler 2014; Nash and Sutcliffe 1970). The correlation coefficient is given by

$$R = \frac{\sum_{i=1}^{N}\left(P_{o,i}-\overline{P_{o,i}}\right)\left(P_{s,i}-\overline{P_{s,i}}\right)}{\sqrt{\sum_{i=1}^{N}\left(P_{o,i}-\overline{P_{o,i}}\right)^2\sum_{i=1}^{N}\left(P_{s,i}-\overline{P_{s,i}}\right)^2}} \tag{20}$$

The RMSE is able to evaluate the goodness of fit relevant to the peak value and more appropriate metric when the error distribution is found to be Gaussian, whereas RMSE (due to its squaring effects) should be used to assess the errors that are not normally distributed. The RMSE value is given by

$$\mathrm{RMSE} = \sqrt{\frac{1}{N}\sum_{i=1}^{N}\left(P_{s,i}-P_{o,i}\right)^2} \tag{21}$$

The MAE is able to generate the performance index of modeled precipitation and the distribution of the modeling errors (Chai and Draxler 2014), and the MAE value is given by

$$\mathrm{MAE} = \frac{1}{N}\sum_{i=1}^{N}\left|\left(P_{s,i}-P_{o,i}\right)\right| \tag{22}$$

The NSE is used to quantify how well a model simulation can predict the outcome variable, and it is sensitive to extreme values and might yield sub-optimal results when the dataset contains large outliers in it, given as

$$\mathrm{NSE} = 1-\left[\frac{\sum_{i=1}^{N}\left(P_{s,i}-P_{o,i}\right)^2}{\sum_{i=1}^{N}\left(P_{o,i}-\overline{P_{o,i}}\right)^2}\right], \quad \infty \le \mathrm{NSE} \le 1 \tag{23}$$

In the above equations, N is the number of input test samples; $P_{o,\,i}$ and $P_{s,\,i}$ are the observed and modeled ith precipitation, respectively; and $\overline{P_{o,i}}$ and $\overline{P_{s,i}}$ are the average of the observed and modeled precipitation, respectively. The better the performance levels of simulation, the closer the R to 1, MAE to 0, RMSE to 0, and NSE to 1.

3 Results and discussion

3.1 Bias correlation

Figure 4 presents the scatter plots of the mean, standard deviation, lag-one correlation, and cross correlation statistics of the NCEP data and the raw and bias-corrected BCC-CSM1-1M atmospheric variables at multiple (i.e., annual, seasonal, monthly) timescales. In this study, the

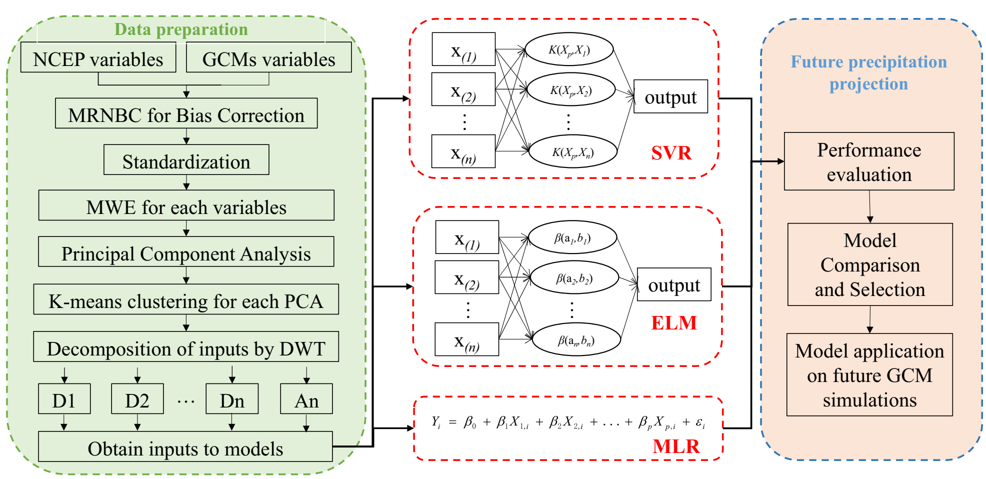

Fig. 3 Flow chart for the downscaling precipitation framework

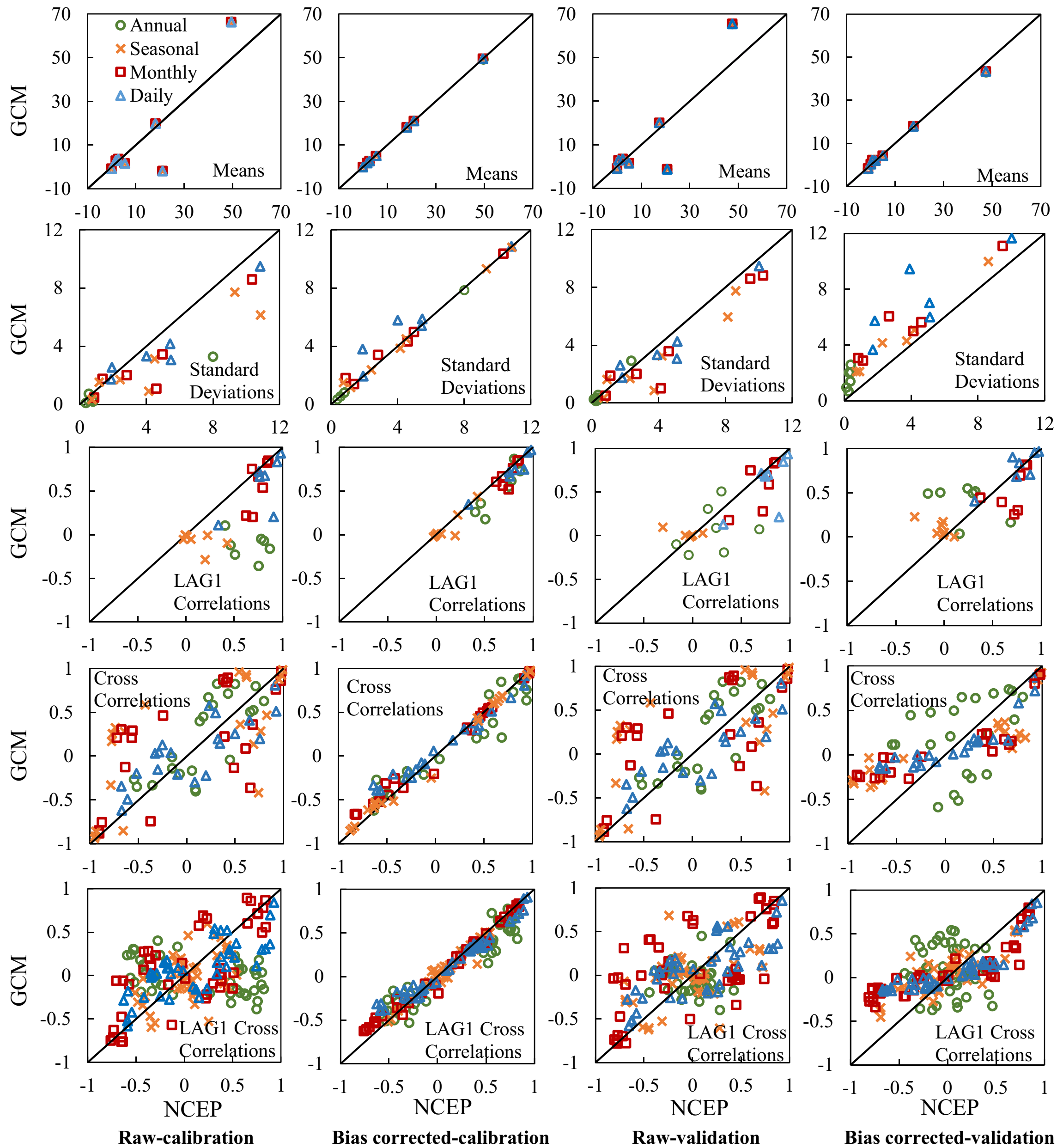

Fig. 4 Scatter plots of the daily, monthly, seasonal, and annual means; standard deviations; lag-one correlation of reanalysis; and the GCM raw and corrected data

number of iterations for recursive scheme of the correction procedure was set to 3 and a total of seven identified atmospheric variables had been taken from the BCC-CSM1-1M models and compared in terms of the results of the raw and corrected models with reanalysis data as an example to illustrate the utility of the proposed approach. The seven variables were the following: Pr, T_{as}, R_{hum}, H_{fls}, R_{lds}, U_{as}, and V_{as}. As expected, the MRNBC clearly shown improvements in the representation of the statistic of each of the predictors compared to the raw GCM simulation for the current climate, providing a good fit to all statistics (including cross and lag-one cross dependence attributes) at all analyzed timescales. However, there were some remaining biases in the variance and persistence compared to the mean correction, especially at annual and seasonal timescales in the validation period, which is primarily due to the complexity of multivariate connections applied among the inter-variable relationships.

To assess closely the implications of bias correction procedure on the distribution, it is important to examine the empirical distribution of reanalysis data and raw and corrected results of GCM at daily, monthly, seasonal, and annual timescales. In accordance with similar information conveyed by the large number of variable plots, we only selected precipitable water to present the corrected results. The raw GCM data exhibited significant biases compared to the reanalysis data with the variable, the timescale, and the exceedance probability. After the bias correction procedure, the performance levels of the corrected GCM data showed good correspondence to the reanalysis data with similar distribution behavior as stimulated in Fig. 5.

3.2 Modeling verification and comparison

In order to verify whether the MRNBC and MWE methods can significantly increase the MLR model's accuracy, we integrated the two methods into four combination methods by establishing the relation between the precipitation and the corrected GCM output atmospheric predictors with the training period of 1960 to 1990 and the validation period of 1991 to 2005. Following this, we selected eight relatively high-spatial resolution GCM model outputs to test the general applicability and to reduce the uncertainty in the downscaled results. Table 3 shows the results of the performance criteria derived from a combination of MRNBC and MWE for eight selected GCM outputs. It is clearly visible that the use of MWE procedure was able to increase the accuracy of the MLR model simulations quite significantly (i.e., with a larger value of NSE and smaller values of RMSE/MAE compared to the performance levels without using MWE) among the eight GCM outputs. By contrast, the MRNBC method did not exhibit an apparent increase in the accuracy of the MLR model, and in fact, the performance of some GCM models was

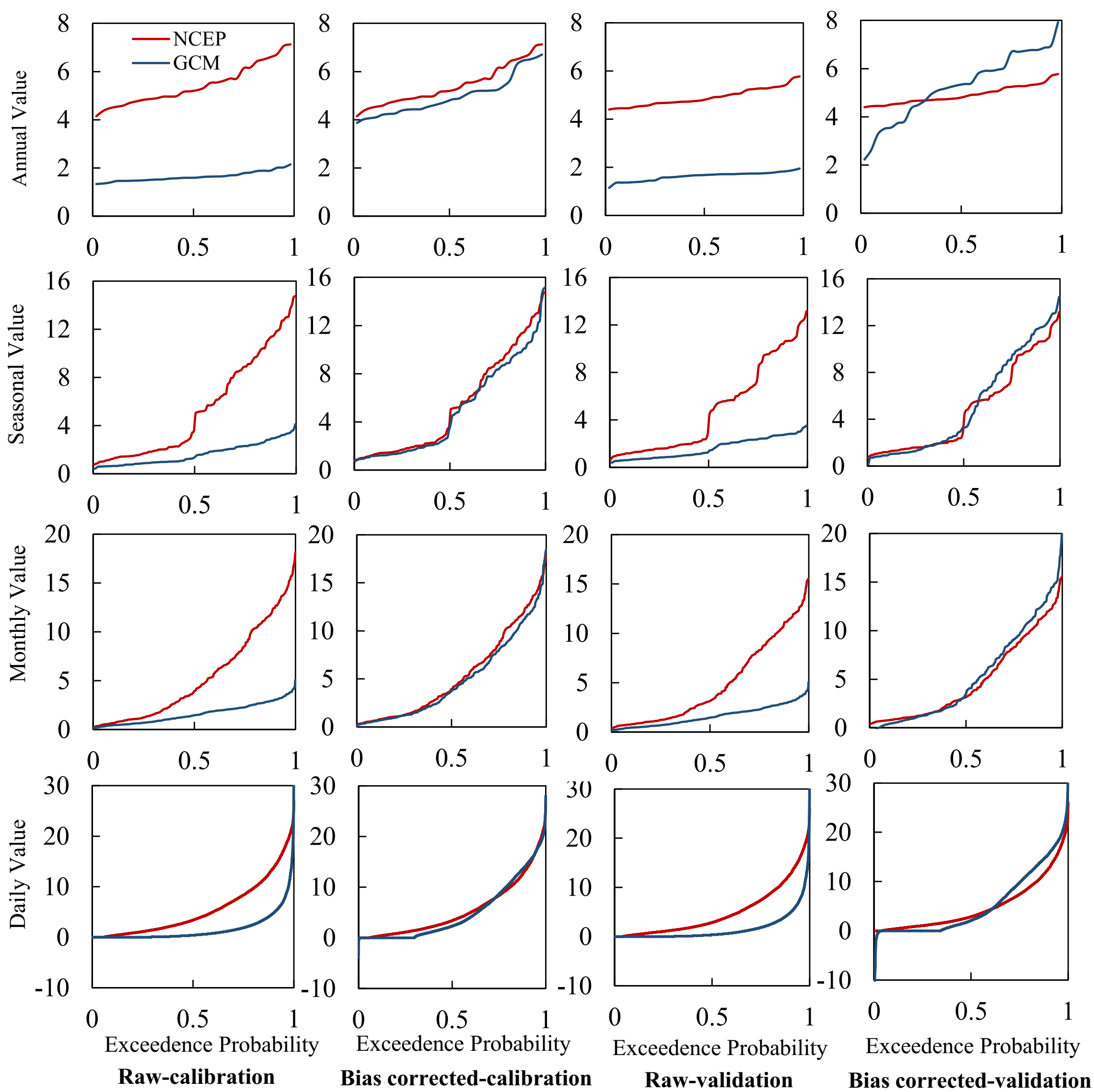

Fig. 5 Empirical distributions of selected multivariate recursive nesting bias correction (MRNBC) corrected and raw variable compared to reanalysis variable at different timescales

Table 3 Performance of the combinations of multivariate recursive nesting bias correction (MRNBC) and multiscale wavelet entropy (MWE) in terms of the MLR simulation in the validation period

GCM	MRNBC	MWE	*R*	NSE	RMSE	MAE
ACCESS1-0	N	N	0.83	0.48	22.43	16.43
	N	Y	0.89	0.75	17.82	12.41
	Y	N	0.83	0.60	22.44	16.25
	Y	Y	0.89	0.74	17.81	12.40
ACCESS1-3	N	N	0.77	0.50	25.25	17.76
	N	Y	0.90	0.75	17.39	12.34
	Y	N	0.83	0.70	22.02	15.85
	Y	Y	0.90	0.76	17.48	12.03
BCC-CSM1-1M	N	N	0.90	0.75	17.39	12.34
	N	Y	0.89	0.75	17.97	12.34
	Y	N	0.85	0.54	21.26	15.08
	Y	Y	0.89	0.73	17.97	12.63
CNRM-CM5	N	N	0.88	0.68	19.16	12.86
	N	Y	0.90	0.76	17.24	11.55
	Y	N	0.88	0.67	19.20	12.90
	Y	Y	0.90	0.76	17.27	11.57
HadGEM2-CC	N	N	0.86	0.60	20.70	15.09
	N	Y	0.90	0.76	17.48	11.85
	Y	N	0.87	0.63	20.06	14.64
	Y	Y	0.90	0.76	17.62	12.05
HadGEM2-ES	N	N	0.85	0.60	20.77	14.79
	N	Y	0.89	0.75	18.04	12.11
	Y	N	0.85	0.59	20.90	14.88
	Y	Y	0.89	0.74	18.07	12.13
MIROC5	N	N	0.88	0.67	19.26	13.70
	N	Y	0.90	0.77	17.63	12.24
	Y	N	0.88	0.68	19.20	13.67
	Y	Y	0.90	0.77	17.67	12.28
MRI-CGCM3	N	N	0.86	0.65	20.26	13.86
	N	Y	0.88	0.73	18.51	12.67
	Y	N	0.86	0.65	20.29	13.88
	Y	Y	0.88	0.73	18.53	12.68

N denotes without using the corresponding method; Y denotes using the corresponding method

worse than those without this procedure. For instance, the performance levels of BCC-CSM1-1M and HadGEM2-ES appeared to decrease as evidenced by a lower value of NSE and larger values of RMSE/MAE relative to the MRNBC method.

It is clearly visible that the use of MWE procedure was able to increase the accuracy of the MLR model simulations quite significantly (i.e., with a larger value of NSE and smaller values of RMSE/MAE compared to the performance levels without using MWE) among the eight GCM outputs. By contrast, the MRNBC method did not exhibit an apparent increase in the accuracy of the MLR model, and in fact, the performance of some GCM models was worse than those without this procedure. For instance, the performance levels of BCC-CSM1-1M and HadGEM2-ES appeared to decrease as evidenced by a lower value of NSE and larger values of RMSE/MAE relative to the MRNBC method.

In light of the above evidence, we deduce that although the MRNBC procedure can obviously correct the bias existing between the NCER/NCEP reanalysis data and the GCM model outputs, the performance levels of the downscaled models did not respond to these bias corrections. A plausible reason for this is because the MRNBC method generally aims to adjust the magnitude and distribution of the GCM outputs and the corrections largely rely on the reanalysis datasets. However, it should be noted that the downscaling point was located in the high upstream where the observation sites are sparse, so the reanalysis data itself is likely to contain a certain degree of bias regarding real situation at that location.

In order to integrate a comparison of the simulation performance of MLR, ELM, and SVR using and without using MRNBC and MWE methods, we figured a box plot of modeling performance levels for each model under the eight given GCMs (Fig. 6). We can see that using MRNBC and MWE methods can dramatically improve the simulation performance of MLR, ELM, and SVR, with increasing *R* and NSE values and decreasing RMSE and MAE values, especially for MLR. It should be noted that using the MRNBC and MWE can significantly decrease the predictive uncertainty that comes from different GCMs because the MRNBC and MWE correct the GCM bias on the target of NCER reanalysis datasets, which means the different corrected GCMs contained the same NCER reanalysis data information, reflected by the simulation performance levels under the given GCMs showing little variations, especially for SVR. It indicates the MRNBC and MWE methods can dramatically increase the simulation performance and decrease the projection uncertainty.

Further, we compared the performance levels of the MLR, SVR, and ELM by using the MRNBC and MWE methods to confirm the satisfactory modeling performance levels for forecasting the precipitation in the future. Figure 7 shows the results of the performance criteria derived from the three models for eight selected GCM outputs. Generally, it is noteworthy that there are obvious different performance levels between MLR and AI-based models (ELM and SVR). For the eight GCM outputs, the precipitation derived from the MLR revealed mediocre performance with the *R* value below 0.9, NSE below 0.77, RMSE above 17 mm/month, and MAE above 11 mm/month. The downscaled precipitation results from the SVR and ELM revealed relatively good performance levels with the *R* values being greater than 0.90, NSE

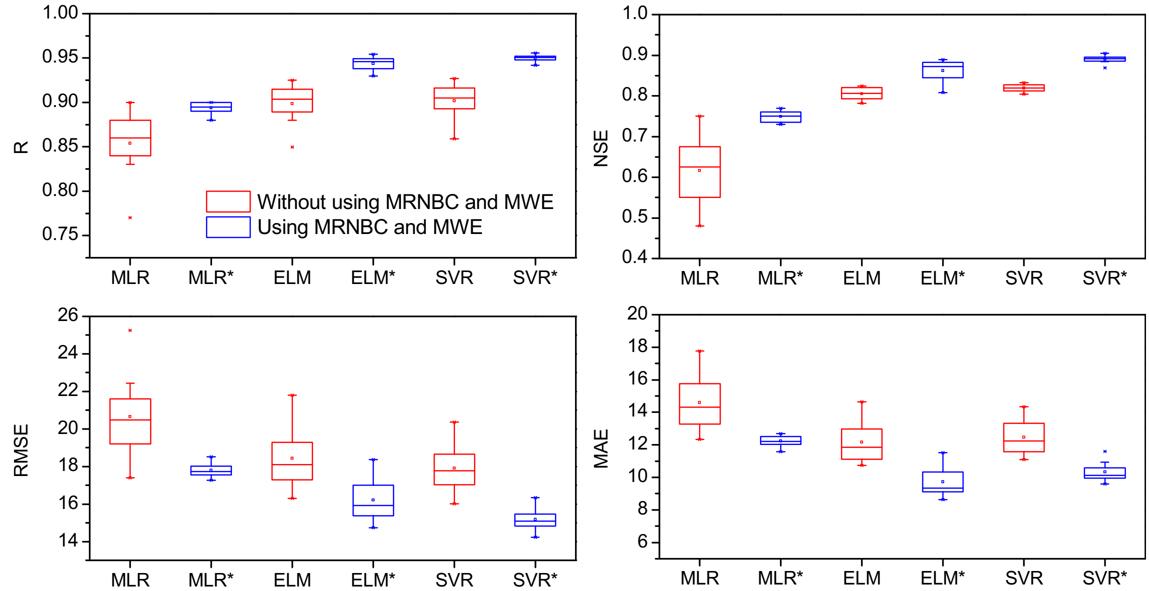

Fig. 6 Box plot for MLR, ELM, and SVR performance comparison using and without using the MRNBC and MWE methods under eight GCMs. Asterisks in the *X*-axis represent using the MRNBC and MWE methods

values being greater than 0.8, and RMSE and MAE values being lower than 18 mm/month and 12 mm/month, respectively. Leaving the performance levels from the SVR and ELM derived by the ACCESS1-0 and ACCESS1-3 alone, the rest six GCMs forced SVR and ELM downscaling precipitation registered much higher performance levels than MLR.

Figure 8 describes a Taylor diagram depicting a joint assessment of SVR, ELM, and MLR models for precipitation simulation horizon. Note that the Taylor plot

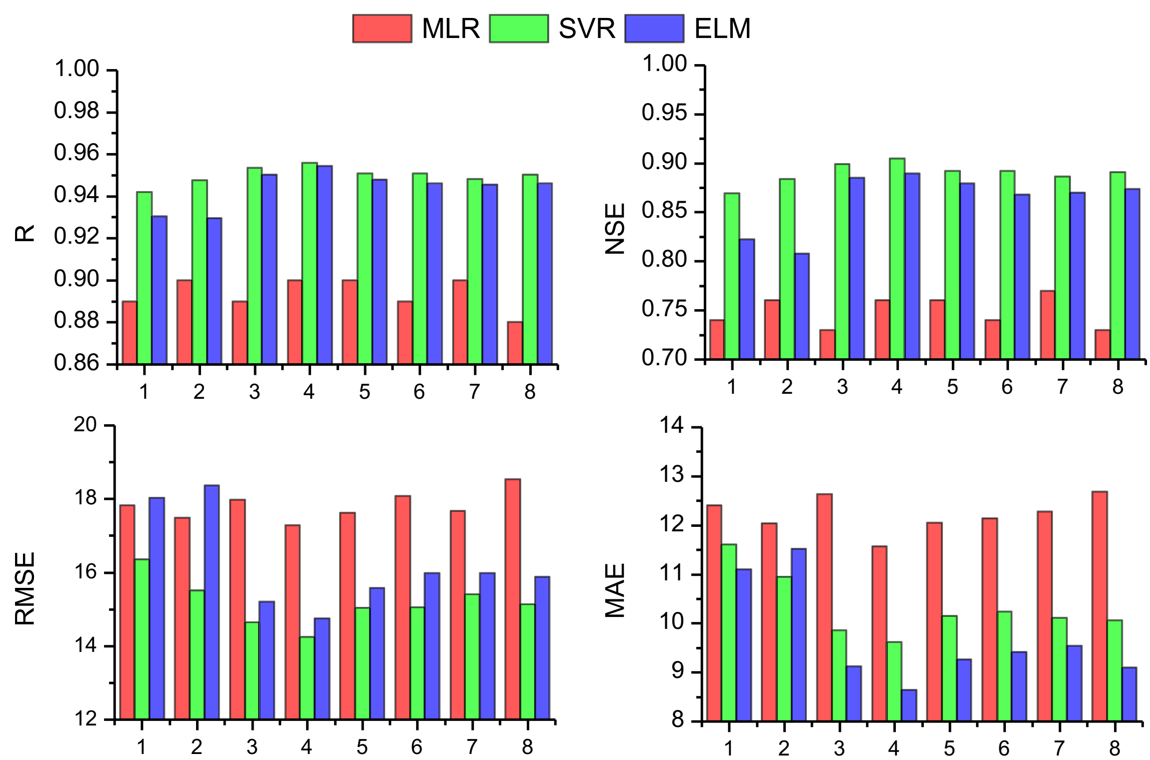

Fig. 7 Performance criteria derived from the eight selected GCM outputs by MLR, SVR, and ELM. The number of *X*-axis label represents the GCM models shown in Table 1

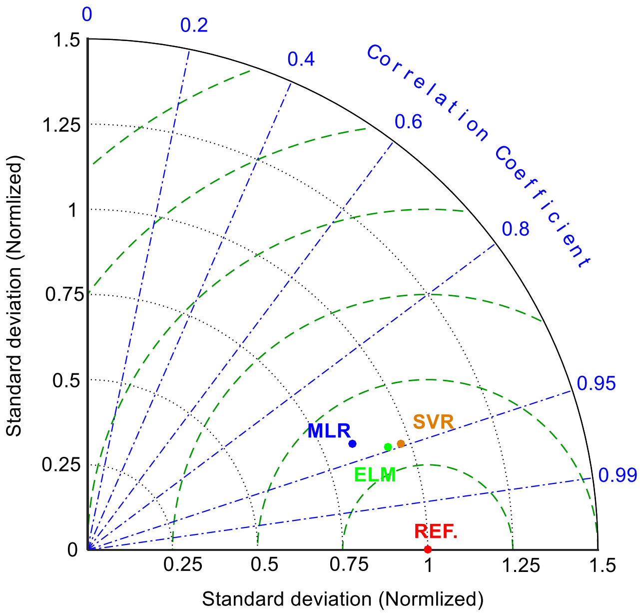

Fig. 8 Taylor diagram of the comparison of MLR, ELM, and SVM performance with an ensemble of GCMs

compares the simulations in respect to a reference, which is the observed data (Taylor 2001; Taylor et al. 2016). This summarizes graphically how closely the simulations match the observations in terms of correlation, centered root-mean-square difference, and the amplitude of variation (represented by standard deviation), as a useful measure in evaluating multiple aspects of models and gauging the relative skill of many different models. There is no doubt that the SVR model is located much closer to the observed reference point, but at the same time, it occupies a larger correlation value with a smaller centered root-mean-square difference and closer standard deviation to the reference. However, the MLR model lies much farther to the line representing the centered root-mean-square difference, while the standard deviation of the MLR model remains modestly farther than both the SVR and ELM models to reference. Thus, we can conclude that the AI-based data-driven models show more accuracy of downscaling precipitation than MRL, which is mainly due to the nonlinearity relationship between atmospheric predictors and precipitation.

When the ELM and SVR model performance levels were compared, the results showed that GCM model outputs from the SVR-based calculations were better than those in respect to the ELM-based calculations, with higher NSE and R values and lower RMSE values (Fig. 7), and the SVR is located closer to the standard deviation line of reference point in the Taylor diagram (Fig. 8). This indicates the SVR model had a better performance compared to the ELM model when applied for downscaling the precipitation data for the mountainous inland watershed region in Northwest China.

Figure 9 reveals the GCM-driven monthly distribution of the precipitation downscaled by the SVR and ELM using MRNBC and MWE methods with 75% predictive uncertainty and compared with the observation. There is distinctly larger uncertainty for the ELM modeling results than SVR, especially during the spring and summer from the May to August. The average precipitation driven by eight GCMs showed consistency to the observational precipitation across the annual timescale, while the precipitation in July calculated by ELM was underestimated more than that by SVR, when compared to observation. It again strengthened the much more good performance of SVR than ELM in dealing with the future precipitation downscaling.

Existing methods try to project future precipitation as accurately as possible. For example, Sehgal et al. (2018) applied the MWE and ANN methods to improve the precipitation projection in the Krishna Basin. Comparing the performance of their work, our study presents more precision with R^2 around 0.9. Due to the only one GCM selected in their work, in our study, we selected eight relatively high-resolution GCMs and applied the MRNBC to reduce the uncertainty from the different GCMs. The results of our study show

Fig. 9 GCM-driven monthly distribution of precipitation downscaled by ELM and SVR with 75% uncertainty and comparison to the observation

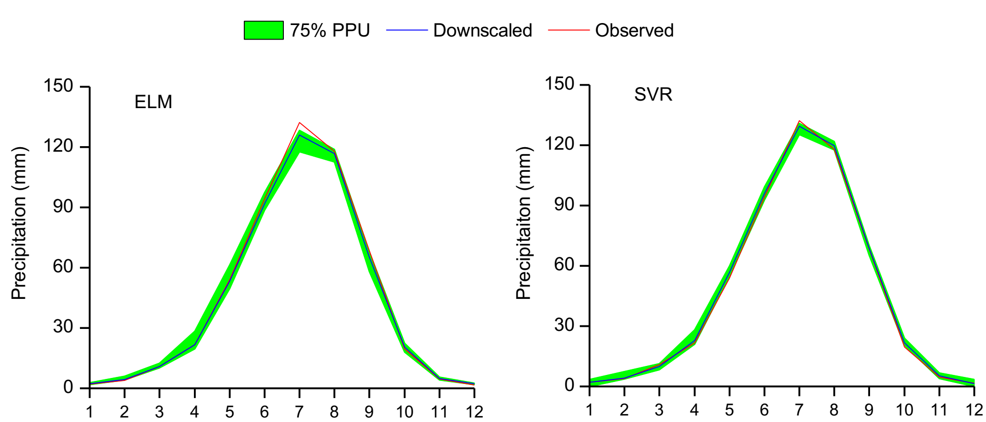

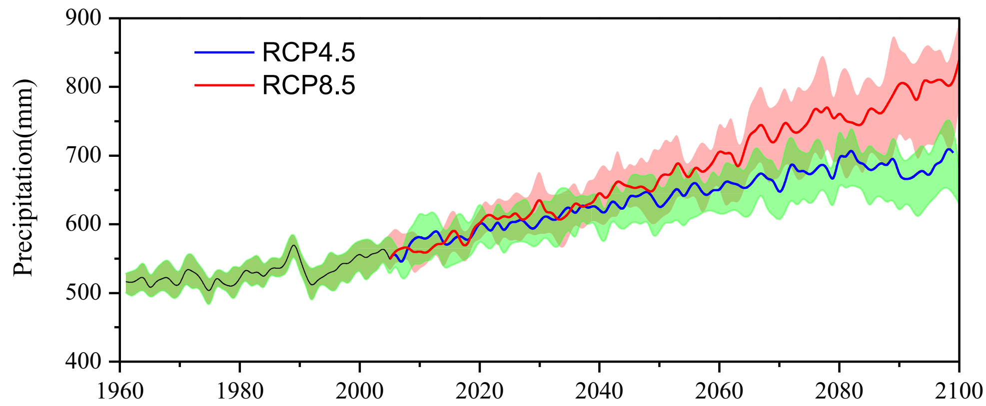

Fig. 10 Annual precipitation variations from 1961 to 2100 averaged over the eight GCM-derived series under the RCP4.5 and RCP8.5 warming scenarios with 75% uncertainty

more robustness and plausibility. Sarhadi et al. (2017) tried the supervised PCA and SVR methods to project precipitation for 15 GCMs with the maximum NSE of 0.78, which is far below than that in our study by applying MRNBC, MWE, and SVR with the average NSE of 0.9. It indicates our downscaling framework is more precise than the existing methods in terms of simulation performance.

3.3 Future precipitation forecasts

We applied the SVR and ELM by using MRNBC and MWE methods to project future precipitation acquired from the eight GCM outputs. Figure 10 shows the variation in precipitation variations from 1961 to 2100 averaged over the eight GCM-derived series for two models under the RCP4.5 and RCP8.5 warming scenarios. Evidently, there is a significant degree of variation in the future precipitation projections under the two warming scenarios. The precipitation variation under the RCP4.5 was relatively moderate when compared with the RCP8.5 scenario. Compared to RCP4.5, the RCP8.5 scenario revealed more obvious rising in precipitation in the future. In the near term (2010–2040), the precipitation under the two scenarios is equivalent with the value of 590 mm, while at the end of the twenty-first century, the projected precipitation under the RCP4.5 scenario tends to be stable while the projected precipitation under the RCP8.5 scenario continues to increase with a larger degree of uncertainty. The precipitation in the long term (2050–2100) is 710 mm under RCP8.5 and 630 mm under RCP4.5. This implies that the future precipitation variation under the RCP8.5 scenario is more significant than that under the RCP4.5 scenario in the present study. The above analysis therefore indicates that the precipitation variation and uncertainties involved generally an increase with an increase in radiative forcing implemented in the RCP8.5 scenario.

In order to compare the relative change in the historical precipitation, we have taken the sub-period 1961 to 2005 as the baseline to incorporate the contribution of climate change to the future precipitation. From Fig. 11, we can see the increasing precipitation in all time periods and scenarios when compared to the historical period. The precipitation in the 2020–2050 increases by 15% under the RCP4.5 scenario and by 19% under the RCP8.5 scenario. For the long-term period 2060–2090, the precipitation projections show increasing trends compared to the historical period. Notably, the increase in precipitation under the RCP8.5 scenario is more

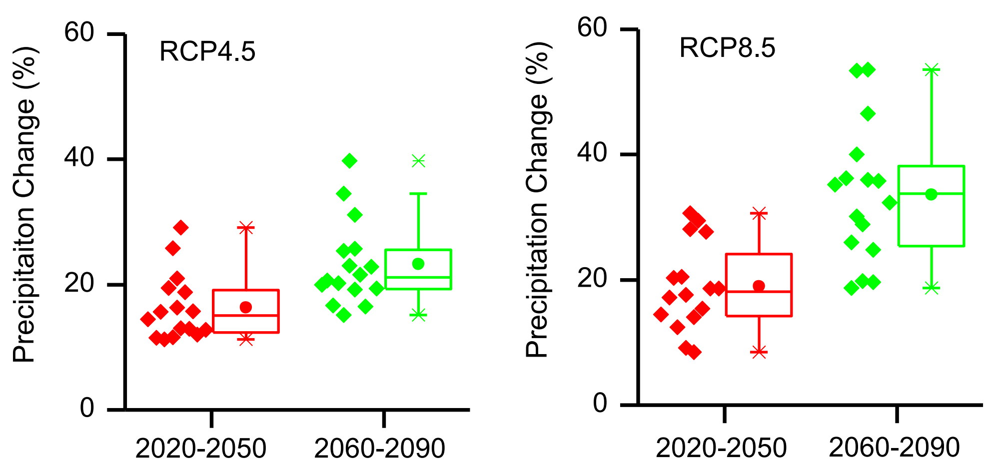

Fig. 11 Precipitation change under two scenarios in different periods relative to 1961–2005

Fig. 12 Monthly slope trends of future precipitation with 75% uncertainty under two periods and two scenarios in upstream of the Heihe River

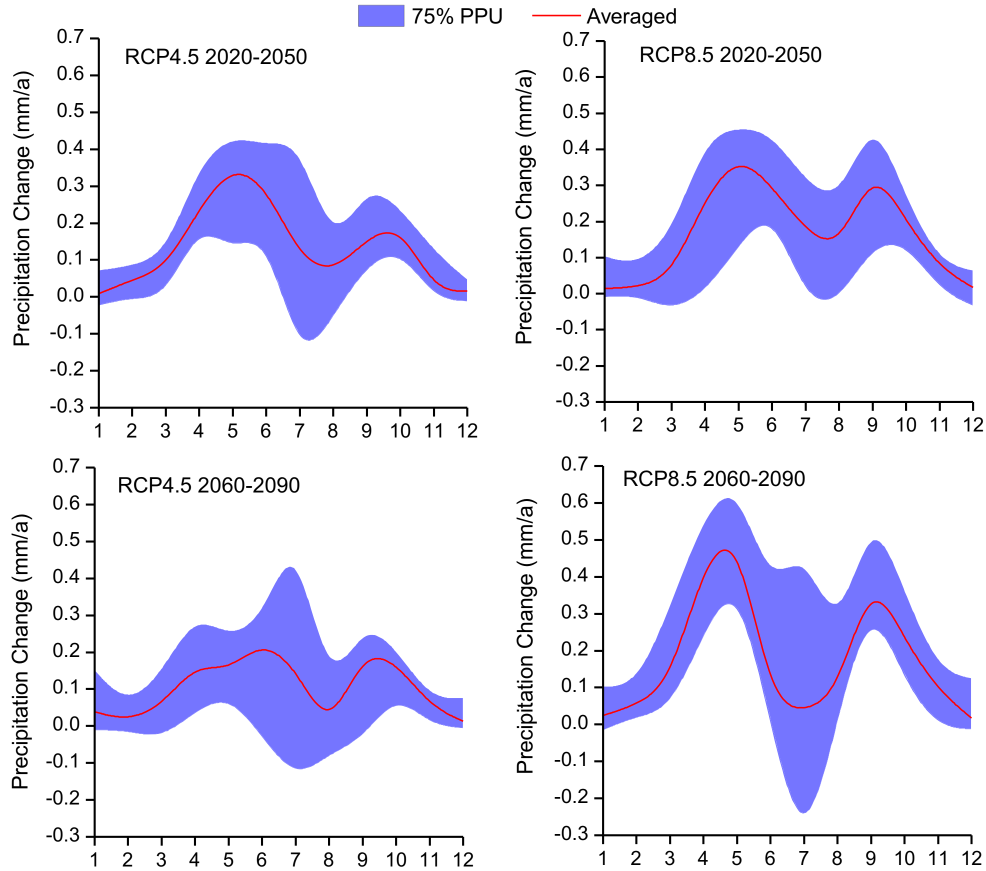

apparent than that under the RCP4.5 scenario, with an average of about 33% vs. 21%.

Figure 12 shows the estimated monthly slopes of the trend generated from the eight GCM-derived projection precipitations under different periods and warming scenarios. It is evident that the slope trends in all months during the whole periods under both scenarios are increasing, and a more apparent increase occurred from April to June and from September to October with rates over 2 mm/10a in the near term of RCP4.5 and the whole period of RCP8.5. The precipitation in winter and summer (July to August) appeared to increase slightly with rates below 1 mm/10a under all periods and scenarios; thus, we can conclude the future precipitation increase is mainly contributed by the fast rising precipitation in spring and autumn.

4 Conclusion

This study has documented the performance of multivariate recursive nesting bias correction (MRNBC) and multiscale wavelet entropy (MWE) applied to remove the discrepancy between the predictors in the simulated GCM and the NCEP reanalysis data and improve the projected future precipitation accuracy of MLR, SVR, and ELM simulations in the upstream of the Heihe River. A total of eight relatively high-spatial resolution GCM outputs from the CMIP5 ESMs were employed to downscale for the historical 1960–2005 and the future period (2010–2100) under the RCP4.5 and RCP8.5 scenarios. The following conclusions can be drawn:

The combination of MRNBC and MWE methods can dramatically increase the simulation performance and reduce the projection-predictive uncertainty from different GCMs. Verified by statistical score metrics applied for evaluation of the results, the developed method appears to be an important statistical tool in the correction of the bias between the GCM output and the reanalysis data. By application of MRL, SVR, and ELM models, the AI-based data-driven methods were found to be efficient for capturing and incorporating physical processes in climatic variables that occur at multiple scales, leading to significant improvements in the predictive performance accuracy of the precipitation projections.

The eight GCM outputs showed a good level of agreement in projecting the future precipitation under the two warming scenarios. The projected precipitation under RCP8.5 appeared to exhibit the significantly increasing trend relative to the

RCP4.5 scenario. In the future, the precipitation will experience an increase by 15–19% from 2020 to 2050 and by 21–33% from 2060 to 2090, compared to the precipitation in 1961–2005.

Acknowledgements The authors thank the anonymous reviewers for their valuable comments and suggestions, which significantly improved this manuscript.

Funding information This study was supported by the National Key R&D Program of China (2017YFC0404302, 2016YFC0400908) and the Key Research Program of Frontier Sciences, CAS (QYZDJ-SSW-DQC031).

References

Abdullah SS, Malek MA, Abdullah NS, Kisi O, Yap KS (2015) Extreme learning machines: a new approach for prediction of reference evapotranspiration. J Hydrol 527:184–195

Agarwal A, Maheswaran R, Kurths J, Khosa R (2016a) Wavelet spectrum and self-organizing maps-based approach for hydrologic regionalization—a case study in the Western United States. Water Resour Manag 30:4399–4413

Agarwal A, Maheswaran R, Sehgal V, Khosa R, Sivakumar B, Bernhofer C (2016b) Hydrologic regionalization using wavelet-based multiscale entropy method. J Hydrol 538:22–32

Asong ZE, Khaliq MN, Wheater HS (2016) Projected changes in precipitation and temperature over the Canadian Prairie provinces using the generalized linear model statistical downscaling approach. J Hydrol 539:429–446

Chai T, Draxler RR (2014) Root mean square error (RMSE) or mean absolute error (MAE)?—arguments against avoiding RMSE in the literature. Geosci Model Dev 7:1247–1250

Dabanlı İ, Şen Z (2017) Precipitation projections under GCMs perspective and Turkish Water Foundation (TWF) statistical downscaling model procedures. Theor Appl Climatol

Deo RC, Şahin M (2016) An extreme learning machine model for the simulation of monthly mean streamflow water level in eastern Queensland. Environ Monit Assess 188:24

Deo RC, Tiwari MK, Adamowski JF, Quilty MJ (2016) Forecasting effective drought index using a wavelet extreme learning machine (W-ELM) model. Stoch Env Res Risk A:1–30

Draper N, Smith H (1981) Applied regression analysis, 709 pp. Wiley, New York

Duhan D, Pandey A (2015) Statistical downscaling of temperature using three techniques in the Tons River basin in Central India. Theor Appl Climatol 121:605–622

Eghdamirad S, Johnson F, Sharma A (2017) Using second-order approximation to incorporate GCM uncertainty in climate change impact assessments. Clim Chang:1–16

Feng Q, Miao Z, Li Z, Li J, Si J, Yonghong S, Chang Z (2015) Public perception of an ecological rehabilitation project in inland river basins in northern China: success or failure. Environ Res 139:20–30

Gocic M, Petković D, Shamshirband S, Kamsin A (2016) Comparative analysis of reference evapotranspiration equations modelling by extreme learning machine. Comput Electron Agric 127:56–63

Gudmundsson L, Bremnes JB, Haugen JE, Engen-Skaugen T (2012) Technical note: downscaling RCM precipitation to the station scale using statistical transformations—a comparison of methods. Hydrol Earth Syst Sci 16:3383–3390

Hamidi O, Poorolajal J, Sadeghifar M, Abbasi H, Maryanaji Z, Faridi HR, Tapak L (2015) A comparative study of support vector machines and artificial neural networks for predicting precipitation in Iran. Theor Appl Climatol 119:723–731

Hartigan JA, Wong MA (1979) A K-means clustering algorithm. Appl Stat 28:100–108

Hassan Z, Harun S (2012) Application of statistical downscaling model for long lead rainfall prediction in Kurau River catchment of Malaysia. Malays J Civil Eng (MJCE) 24:1–12

Huang G-B (2015) What are extreme learning machines? Filling the gap between frank Rosenblatt's dream and John von Neumann's puzzle. Cogn Comput 7:263–278

Huang G-B, Zhu Q-Y, Siew C-K (2004) Extreme learning machine: a new learning scheme of feedforward neural networks, 2004 IEEE International Joint Conference on Neural Networks (IEEE Cat. No. 04CH37541), pp. 985–990; vol. 982

Huang G-B, Zhu Q-Y, Siew C-K (2006) Extreme learning machine: theory and applications. Neurocomputing 70:489–501

Huth R, Beck C, Philipp A, Demuzere M, Ustrnul Z, Cahynová M, Kyselý J, Tveito OE (2008) Classifications of atmospheric circulation patterns. Ann N Y Acad Sci 1146:105–152

Jin X, Han J (2016) K-means clustering. In: Sammut C, Webb GI (eds) Encyclopedia of machine learning and data mining. Springer US, Boston, pp 1–3

Knutti R, Furrer R, Tebaldi C, Cermak J, Meehl GA (2010) Challenges in combining projections from multiple climate models. J Clim 23: 2739–2758

Kouhestani S, Eslamian SS, Abedi-Koupai J, Besalatpour AA (2016) Projection of climate change impacts on precipitation using soft-computing techniques: a case study in Zayandeh-Rud Basin, Iran. Glob Planet Chang 144:158–170

Macqueen J (1967) Some methods for classification and analysis of multivariate observations, Proc. of Berkeley Symposium on Mathematical Statistics and Probability, pp. 281–297

Maheswaran R, Khosa R (2012) Wavelet–Volterra coupled model for monthly stream flow forecasting. J Hydrol 450–451:320–335

Maraun D (2016) Bias correcting climate change simulations—a critical review. Curr Clim Chang Rep 2:211–220

Mehrotra R, Sharma A (2015) Correcting for systematic biases in multiple raw GCM variables across a range of timescales. J Hydrol 520: 214–223

Mehrotra R, Sharma A, Nagesh Kumar D, Reshmidevi TV (2013) Assessing future rainfall projections using multiple GCMs and a multi-site stochastic downscaling model. J Hydrol 488:84–100

Misra V, Dirmeyer PA, Kirtman BP (2003) Dynamic downscaling of seasonal simulations over South America. J Clim 16:103–117

Montgomery DC, Peck EA, Vining GG (2012) Introduction to linear regression analysis. Wiley

Nash J, Sutcliffe J (1970) River flow forecasting through conceptual models: part I—a discussion of principles. J Hydrol 10:282–290

Patil AP, Deka PC (2016) An extreme learning machine approach for modeling evapotranspiration using extrinsic inputs. Comput Electron Agric 121:385–392

Salas JD, Tabios GQ, Bartolini P (1985) Approaches to multivariate modeling of water resources time series1. JAWRA J Am Water Resour Assoc 21:683–708

Salvi K, Kannan S, Ghosh S (2013) High-resolution multisite daily rainfall projections in India with statistical downscaling for climate change impacts assessment. J Geophys Res: Atmos 118:3557–3578

Sang Y, Wang D, Wu J, Zhu Q, Wang L (2011) Wavelet-based analysis on the complexity of hydrologic series data under multi-temporal scales. Entropy 13:195–210

Santos JA, Belo-Pereira M, Fraga H, Pinto JG (2016) Understanding climate change projections for precipitation over Western Europe with a weather typing approach. J Geophys Res: Atmos 121: 1170–1189

Sarhadi A, Burn DH, Johnson F, Mehrotra R, Sharma A (2016) Water resources climate change projections using supervised nonlinear and multivariate soft computing techniques. J Hydrol 536:119–132

Sarhadi A, Burn DH, Yang G, Ghodsi A (2017) Advances in projection of climate change impacts using supervised nonlinear dimensionality reduction techniques. Clim Dyn 48:1329–1351

Sehgal V, Lakhanpal A, Maheswaran R, Khosa R, Sridhar V (2018) Application of multi-scale wavelet entropy and multi-resolution Volterra models for climatic downscaling. J Hydrol 556:1078–1095

Sillmann J, Kharin VV, Zhang X, Zwiers FW, Bronaugh D (2013) Climate extremes indices in the CMIP5 multimodel ensemble: part 1. Model evaluation in the present climate. J Geophys Res: Atmos 118:1716–1733

Srikanthan R, Pegram GGS (2009) A nested multisite daily rainfall stochastic generation model. J Hydrol 371:142–153

Sturm BL (2007) A wavelet tour of signal processing (review). Comput Music J 31:83–85

Taylor KE (2001) Summarizing multiple aspects of model performance in a single diagram. J Geophys Res: Atmos 106:7183–7192

Taylor KE, Stouffer RJ, Meehl GA (2012) An overview of CMIP5 and the experiment design. Bull Am Meteorol Soc 93:485–498

Taylor M, Kosmopoulos P, Kazadzis S, Keramitsoglou I, Kiranoudis C (2016) Neural network radiative transfer solvers for the generation of high resolution solar irradiance spectra parameterized by cloud and aerosol parameters. J Quant Spectrosc Radiat Transf 168:176–192

Vapnik V (1995) The nature of statistical learning theory. Springer, New York

Wilby RL, Dawson CW (2013) The statistical downscaling model: insights from one decade of application. Int J Climatol 33:1707–1719

Wilks DS (1998) Multisite generalization of a daily stochastic precipitation generation model. J Hydrol 210:178–191

Yang L, Feng Q, Yin Z, Deo RC, Wen X, Si J, Li C (2017a) Separation of the climatic and land cover impacts on the flow regime changes in two watersheds of Northeastern Tibetan Plateau. Adv Meteorol 2017:15

Yang L, Feng Q, Yin Z, Wen X, Si J, Li C, Deo RC (2017b) Identifying separate impacts of climate and land use/cover change on hydrological processes in upper stream of Heihe River, Northwest China. Hydrol Process 31:1100–1112

Yin Z, Feng Q, Yang L, Deo R, Wen X, Si J, Xiao S (2017) Future projection with an extreme-learning machine and support vector regression of reference evapotranspiration in a mountainous inland watershed in North-West China. Water 9:880

View publication stats